

EGS-z11-R0: a red, dust-rich galaxy at Cosmic Dawn

Giulia Rodighiero^{1,2*}, Andrea Ferrara³, Michele Catone^{1,2}, Lorenzo Napolitano⁴, Paolo Cassata^{1,2}, Giovanni Gandolfi⁴, Emiliano Merlin², Andrea Grazian², Alvio Renzini², Laura Bisigello², Marco Castellano⁴, Pablo G. Pérez-González⁵, Borja Pérez-Díaz⁴, Edoardo Iani⁶, Carlotta Gruppioni⁷, Steven L. Finkelstein⁸, Anton M. Koekemoer⁹, Alessandro Bianchetti², and Francesco Sinigaglia^{10,11,12,13}

¹ Dipartimento di Fisica e Astronomia "G. Galilei", Università di Padova, Vicolo dell'Osservatorio 3, 35131 Padova, Italy

² INAF, Osservatorio Astronomico di Padova, Vicolo dell'Osservatorio 5, 35122 Padova, Italy

³ Scuola Normale Superiore, Piazza dei Cavalieri 7, I-56126 Pisa, Italy

⁴ INAF, Osservatorio Astronomico di Roma, Via Frascati 33, 00078 Monteporzio Catone, Roma, Italy

⁵ Centro de Astrobiología (CAB), CSIC-INTA, Ctra. de Ajalvir km 4, Torrejón de Ardoz, E-28850, Madrid, Spain

⁶ Institute of Science and Technology Austria (ISTA), Am Campus 1, 3400 Klosterneuburg, Austria

⁷ INAF-Osservatorio di Astrofisica e Scienza dello Spazio, via Gobetti 93/3, I-4019, Bologna, Italy

⁸ Department of Astronomy, The University of Texas at Austin, Austin, TX, USA

⁹ Space Telescope Science Institute, 3700 San Martin Drive, Baltimore, MD 21218, USA

¹⁰ Institute for Fundamental Physics of the Universe, Via Beirut 2, I-34151 Trieste, Italy

¹¹ SISSA - International School for Advanced Studies, Via Bonomea 265, 34136 Trieste, Italy

¹² INAF - Osservatorio Astronomico di Trieste, Via G. B. Tiepolo 11, I-34131 Trieste, Italy

¹³ INFN - National Institute for Nuclear Physics, Via Valerio 2, I-34127 Trieste, Italy

Received ; accepted

ABSTRACT

Context. Galaxies discovered by JWST at $z > 10$ are predominantly characterized by extremely blue rest-frame UV slopes, consistent with dust-poor stellar populations. Conversely, the existence of dust-reddened systems at such early epochs has remained largely unconfirmed spectroscopically.

Aims. We present the spectroscopic confirmation of EGS-z11-R0 at $z = 11.45$, the most distant red galaxy identified and confirmed to date. Discovered serendipitously through inspection of publicly available JWST/NIRSpec data, EGS-z11-R0 offers a rare window into early dust and metal enrichment at cosmic dawn.

Methods. We analyze JWST/NIRSpec PRISM and G395M spectroscopy together with multiwavelength *HST*, NIRC*am*, and MIRI photometry. The spectroscopic redshift is derived from rest-frame UV emission lines detected in the NIRSpec PRISM spectrum. In particular, we identify significant detections of the C IV $\lambda\lambda 1548, 1551$ and C III] $\lambda 1908$ transitions, whose line centroids yield a weighted-average redshift of $z_{\text{spec}} = 11.452 \pm 0.021$. We measure rest-frame UV emission-line fluxes and equivalent widths and use these diagnostics to constrain the nature of the ionizing radiation field. Finally, we perform spectral energy distribution (SED) modeling with CIGALE, combining the spectroscopy with broadband photometry and including stellar, nebular, dust, and active galactic nuclei (AGN) components.

Results. EGS-z11-R0 exhibits a red UV continuum slope ($\beta_{\text{UV}} \sim -1.0$), placing it well above the canonical $M_{\text{UV}}-\beta_{\text{UV}}$ relation at $z \sim 10-12$ and making it the highest-redshift spectroscopically confirmed member of the emerging “red monster” population. Emission-line diagnostics reveal a hard ionizing spectrum consistent with extreme star formation and compatible with a composite stellar+AGN scenario. The best-fit SED solution favors a stellar mass of $\log(M_{\star}/M_{\odot}) \sim 9.2-9.6$, a star-formation rate of $\sim 10-40 M_{\odot} \text{ yr}^{-1}$, and substantial dust attenuation ($A_V \sim 1.2$ mag), significantly higher than typical values inferred for the bulk of $z > 10$ galaxies.

Conclusions. The confirmation of EGS-z11-R0 establishes that chemically evolved, dust-enriched galaxies were already in place at $z \sim 11.5$. Its red UV slope demonstrates that rapid metal and dust production occurred within the first few hundred million years of cosmic history. While a moderate AGN contribution cannot be excluded, the data robustly indicate a dust-enriched system observed during an early, possibly obscured phase of galaxy assembly, challenging the prevailing view of an exclusively blue and dust-poor Cosmic Dawn.

Key words. Galaxies: high-redshift – Galaxies: evolution – Galaxies: ISM – Dust, extinction

1. Introduction

The first few hundred million years after the Big Bang represent a critical phase in galaxy formation, when the earliest stellar systems assembled, enriched their interstellar media with heavy elements, and contributed to cosmic reionization. Since its commissioning, the *James Webb Space Telescope* (JWST) has revo-

lutionized our view of this epoch, revealing a surprisingly abundant population of luminous galaxies at $z > 10$, corresponding to cosmic ages $\lesssim 500$ Myr (e.g. Naidu et al. 2022; Harikane et al. 2022; Austin et al. 2023; Castellano et al. 2023; Finkelstein et al. 2024; Pérez-González et al. 2023, 2025; Gandolfi et al. 2025).

A defining characteristic of the majority of these systems is their extremely blue rest-frame ultraviolet (UV) continuum slopes, often reaching $\beta_{\text{UV}} \lesssim -2.5$ (Morales et al. 2024; Austin

* Corresponding author, e-mail: giulia.rodighiero@unipd.it

et al. 2025; Cullen et al. 2024; Marques-Chaves et al. 2026). Such steep slopes are typically interpreted as evidence for young, metal-poor stellar populations with minimal dust attenuation.

However, recent studies have uncovered a small but intriguing population of candidate high-redshift galaxies exhibiting significantly redder UV continua (i.e. $\beta_{UV} > -1.5$, Rodighiero et al. 2023; Mitsuhashi et al. 2025; Donnan et al. 2025; Tang et al. 2025; Kokorev et al. 2025; Napolitano et al. 2025b; Taylor et al. 2025). These objects deviate markedly from the canonical M_{UV} - β_{UV} relation established at $z \sim 6$ -9 and extended to $z \sim 10$ -12 with JWST. The physical origin of such red slopes at $z > 10$ remains uncertain and given the short age of the Universe at these epochs ($\lesssim 400$ Myr), substantial reddening is difficult to reconcile with simple models of chemically primitive galaxies.

However, dust attenuation provides the most direct interpretation, requiring visual extinctions of $A_V \sim 0.5$ -1 mag to reproduce $\beta_{UV} \gtrsim -1.5$. Such values imply rapid metal production and efficient grain growth within the first few hundred million years. Alternatively, strong nebular continuum emission from dense, highly ionized gas can redden the UV spectrum without invoking large dust masses, although reproducing the most extreme slopes requires very high ionization parameters and stellar effective temperatures (Katz et al. 2025). A further possibility is the presence of a hard ionizing source, such as an accreting black hole, contributing to a composite stellar+AGN spectrum (e.g. Hainline et al. 2011, 2012; Napolitano et al. 2025b).

Recent theoretical models provide essential context for these scenarios. Cosmological zoom-in simulations including on-the-fly dust evolution and radiative transfer (e.g. Narayanan et al. 2025) demonstrate that bursty star-formation histories alone can generate a wide range of intrinsic UV slopes ($\beta_0 \sim -3$ to -2.2). However, slopes redder than $\beta_{UV} \sim -1.5$ generally require significant dust attenuation once nebular continuum effects are included (e.g. Katz et al. 2025).

Other models reinforce this picture. Ferrara (2024) proposes that galaxies at $z > 10$ initially undergo radiative feedback-regulated phases leading to a bursty star formation mode. When dust shielding becomes important the galaxy switches to a smooth, substantially obscured star formation regime (that we define here as a "Red Monster" phase). During such obscured phase, lasting $\approx 20\%$ of the galaxy lifetime, $\approx 70\%$ of the observed stars are formed. As the galaxy becomes super-Eddington, a powerful radiation-driven outflow clears most of the dust the galaxy transitions into a "blue monster" dominating the bright end of the UV luminosity function.

Other theoretical frameworks have also explored the rapid buildup of galaxies at cosmic dawn. In particular, Dekel et al. (2023) proposed a feedback-free model in which the early growth of galaxies is driven by intense cold gas inflows and sustained star formation, with feedback playing a limited role during the first stages of galaxy assembly. In this scenario, the efficient accretion of baryons allows galaxies to rapidly build up their stellar mass already within the first few hundred million years after the Big Bang. On the other hand, Somerville et al. (2025) investigated the early evolution of galaxies within cosmological semi-analytic models that implement a density-regulated star formation framework, in which the efficiency of star formation and feedback processes is governed by the gas density and the physical conditions of the interstellar medium.

Furthermore, observational evidence increasingly points toward rapid early stellar assembly of galaxies at these epochs. Santini et al. (2025) show that several $z > 10$ systems exhibit unexpectedly high stellar masses, mass-to-light ratios, and specific star-formation rates (sSFR), indicating that substantial stellar as-

sembly has already occurred within the first few hundred million years. The apparent lack of strong sSFR evolution at $z > 9$ suggests efficient and sustained star formation, possibly occurring during dust-obscured phases predicted by theoretical models. Together, these results imply that red, dust-reddened sources may represent a fundamental and common stage in early galaxy growth rather than rare anomalies.

Despite these theoretical and observational indications, robust spectroscopic confirmation of strongly dust-reddened galaxies at $z > 10$ are still lacking. Most red candidates identified so far rely on broadband photometry, where degeneracies between dust, age, nebular emission, and AGN activity complicate the interpretation. Secure spectroscopy is therefore essential to establish whether chemically evolved, dust-enriched galaxies were already in place within the first ~ 400 Myr of cosmic history.

In this work, we present the spectroscopic confirmation of EGS-z11-R0 at $z = 11.45$, currently the most distant red galaxy identified and confirmed to date. The source was discovered serendipitously through visual inspection of publicly available JWST/NIRSpec data in the CEERS field. EGS-z11-R0 exhibits a remarkably flat UV continuum slope ($\beta_{UV} \sim -1.0$), placing it well above the canonical M_{UV} - β_{UV} relation at $z \sim 10$ -12. We detect some high-ionization UV emission lines.

We investigate whether the red UV slope of EGS-z11-R0 is primarily driven by dust attenuation associated with rapid chemical enrichment, extreme nebular emission powered by dense star formation, or a composite stellar+AGN ionizing spectrum. Combining NIRSpec spectroscopy with multiwavelength HST, NIRCам, and MIRI photometry, we perform SED modeling including stellar, nebular, dust, and AGN components. Our goal is to assess whether EGS-z11-R0 represents an early, chemically evolved system observed during a short-lived, obscured phase of galaxy assembly at cosmic dawn.

This Letter is structured as follows. Section 2 describes the target selection and spectroscopic data. Section 3 presents the UV slope measurements and their placement in the M_{UV} - β_{UV} plane. Section 4 investigates emission-line diagnostics to constrain the nature of the ionizing source. Section 5 discusses SED modeling results and the role of dust and AGN contributions. We conclude with implications for early metal enrichment and the emerging population of "red monsters" at Cosmic Dawn.

Throughout this work, we adopt the cosmological parameters yielded by the latest Planck collaboration release (Planck Collaboration et al. 2020) and a Chabrier (2003) initial mass function (IMF).

2. Target selection

The source analyzed in this work was initially identified through a visual inspection of publicly available JWST spectroscopic products in the DAWN JWST ARCHIVE (DJA¹, Heintz et al. 2024; de Graaff et al. 2025). During a systematic search for extreme $z > 10$ candidates, we specifically selected objects displaying unusually red rest-frame UV continua compared to the bulk of blue, dust-poor galaxies commonly found at similar epochs. EGS-z11-R0 stood out for its markedly red UV slope, inferred from the NIRSpec continuum, and it exhibits a clear dropout in the bluest region of the spectrum, consistent with a Lyman break at $z > 11$. It is located in the CEERS field (Finkelstein et al. 2025a), at RA = 14^h : 19^m : 26.^s81, DEC = 52° : 51' : 42."66 with a reported spectroscopic redshift of $z_{\text{spec}} = 11.4395$ (JWST

¹ <https://dawn-cph.github.io/dja/>

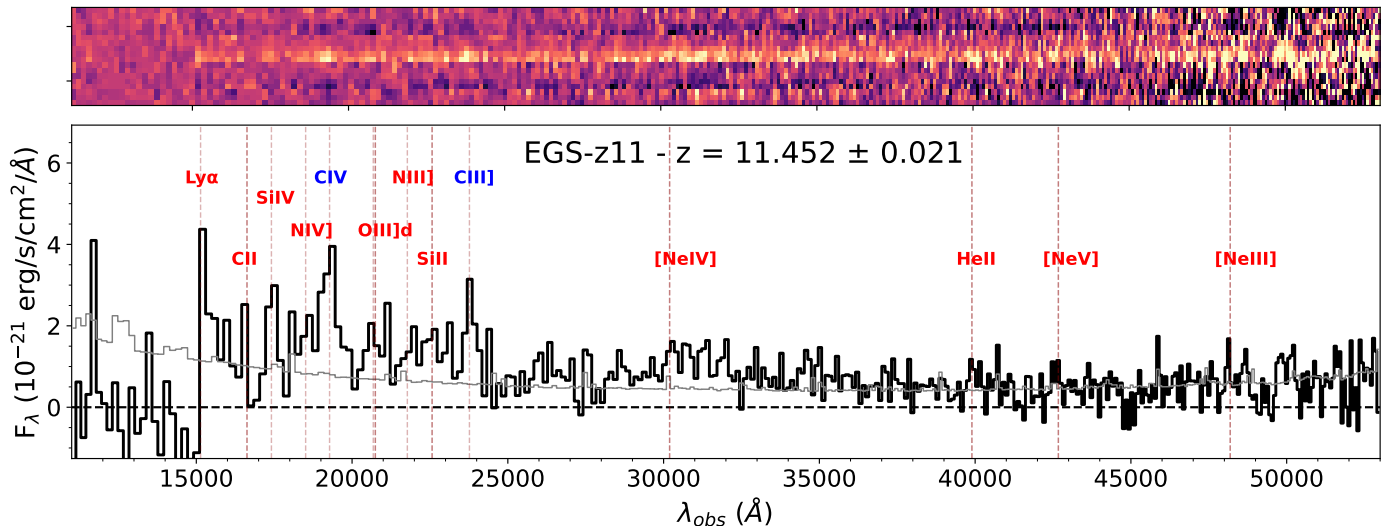


Fig. 1. Observed 2D spectrum (top panel) and extracted 1D spectrum (bottom panel) of EGS-z11-R0. The pipeline-provided error spectrum is shown in light gray. Emission lines with integrated S/N > 3 are highlighted in blue, while the locations of lines for which only a 3σ upper limit is obtained are marked in red.

GO program 4106, P.I.E. Nelson, DJA srcid = 60147). The target has been acquired in two MSA/NIRSpec configurations: 1) a low resolution PRISM (R~100) observation (exposure time 13130 sec); 2) a medium resolution G395M_F290LP (R~1000, exposure time 3130 sec) spectrum covering the range of 2.87-5.14 μm . We adopt the spectra reduced with the public DJA pipeline (v4)².

2.1. NIRSpec spectral analysis

We visually inspected the NIRSpec PRISM spectrum (Fig. 1) at the initial redshift solution $z_{\text{spec}} = 11.4395$ suggested by DJA and searched for the Ly α -break and emission lines features to measure the spectroscopic redshift and emission lines. We followed the same approach described in Napolitano et al. (2025a) and considered as significant only integrated line emissions with a S/N > 3, accounting for errors in both the integrated line flux and the extrapolated continuum at the line position. In particular, the continuum was estimated through a linear interpolation of regions closest to each line that are free from potential features, using the EMCEE (Foreman-Mackey et al. 2013) to perform a Markov chain Monte Carlo (MCMC) analysis. To determine a first estimate of line fluxes, we directly integrated the continuum-subtracted spectrum within a window centered at the expected observed wavelength and spanning $4 \times \sigma_R(\lambda)$, where $\sigma_R(\lambda)$ represents the expected Gaussian standard deviation for a line observed at resolution $R(\lambda)$. The resolution is provided by the JWST documentation³ with the assumption of a source that illuminates the slit uniformly. Only the UV carbon transitions CIV $\lambda\lambda 1548, 51$ and CIII] $\lambda 1908$ in the PRISM spectrum were found as significant with S/N = 3.9 and 3.2, respectively. We recomputed the spectroscopic redshift by taking a weighted average of the line centroids from the carbon emission lines only and found $z_{\text{spec}} = 11.452 \pm 0.021$, adopted as reference hereafter. We note this value matches the DJA redshift estimate within 1σ

uncertainty.

As detailed in Castellano et al. (2024), for the two significant emission features, we then performed a Gaussian fit on the continuum-subtracted flux using the SPECUTILS package of ASTROPY (Astropy Collaboration et al. 2013) to obtain a flux and rest-frame equivalent widths (EW) measurements. The mean of the Gaussian was allowed to vary with $\Delta z = 0.04$, and the Gaussian standard deviation within 5% of the nominal $\sigma_R(\lambda)$, to account for redshift uncertainties. We further refined the Gaussian fit by employing an MCMC analysis with EMCEE. The amplitude, standard deviation and their uncertainty obtained from the best Gaussian model outputted by the SPECUTILS package were used to initialize 100 walkers with 100,000 iterations. The best model parameters and the integrated flux were determined by taking the median of the posterior distributions resulting from the MCMC fitting routine. Uncertainties were calculated based on the 68-th percentile highest posterior density intervals. EW and their uncertainties were computed based on the integrated flux, the continuum flux determined at the line's position, and the spectroscopic redshift. We present the best fit models in Fig. 2 (top and middle panels) and report line measurements in Table 1. We did not significantly detect any other UV emission lines from direct integration. In Table 1 we reported a 3σ upper limit for the He II $\lambda 1640$ which is relevant for the analysis in Sect. 4.

Following Napolitano et al. (2025c), we estimated the UV slope β_{UV} by fitting a power-law model ($f_\lambda \propto \lambda^\beta$) to the continuum flux in the rest-frame range 1350–2600 \AA of the NIRSpec PRISM spectrum. To avoid line contamination, we masked the CIV $\lambda\lambda 1548, 51$ and CIII] $\lambda 1909$ features using line widths broadened according to the instrumental resolution. The fitting is performed using the EMCEE with 30 walkers and 500,000 steps and adopting a flat prior on β_{UV} between -3.5 and 0. We found $\beta_{\text{UV}} = -0.68 \pm 0.30$, where the best-fit value and uncertainty are derived from the posterior median and standard deviation, respectively.

A full characterization of the various lines and their significance will be discussed in Sect. 4.

² <https://dawn-cph.github.io/dja/spectroscopy/nirspec/>

³ <https://jwst-docs.stsci.edu/jwst-near-infrared-spectrograph/nirspec-instrumentation/nirspec-dispersers-and-filters>

Table 1. Emission-line measurements for EGS-z11-R0.

Line	Flux (10^{-21} erg s $^{-1}$ cm $^{-2}$)	EW $_0$ (Å)
C IV $\lambda\lambda 1548, 51$	1399.0 ± 359.1	95.1 ± 26
He II $\lambda 1640$	< 537	–
C III] $\lambda 1908$	623.3 ± 193.1	46.9 ± 14.1

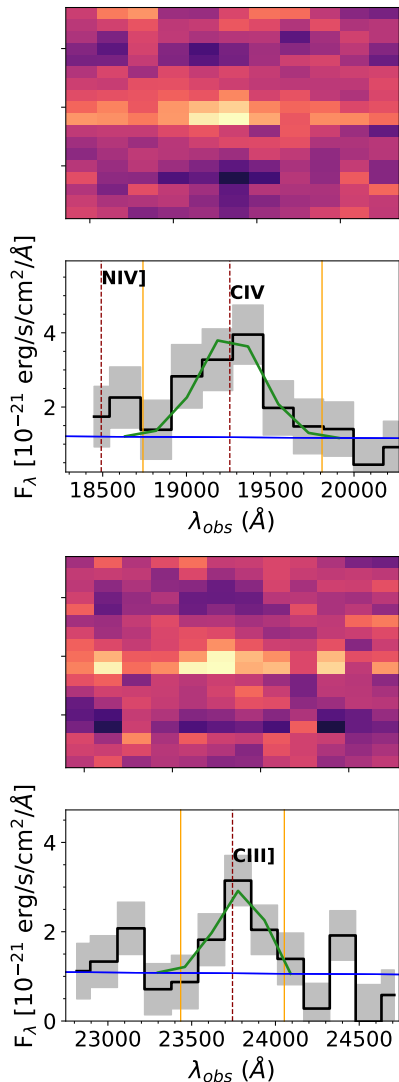


Fig. 2. Top and bottom panels: Rest-frame UV spectral regions of EGS-z11-R0 extracted from the NIRSspec prism data. Zoom-in around the C IV emission feature and the C III] doublet, respectively. The gray curves show the observed spectrum, while the shaded regions represent the 1σ uncertainties.

2.2. Photometry

EGS-z11-R0 has been identified in v1.0 of the public Cosmic Evolution Early Release Science (CEERS; Finkelstein et al. 2025b; Bagley et al. 2023) survey’s photometric catalog (Cox et al. 2025) as source ID 19266, as well as in v0.5 of the UNICORN catalog (Finkelstein et al. 2025, in prep.; ID 88738), and in the ASTRODEEP-JWST catalog (Merlin et al. 2024) as source ID CEERS-77458. We exploit JWST/NIRCam measurements from the v1.0 CEERS catalog, and combine these with NIRCam F090W and other photometry from the v0.5 UNICORN catalog, which includes HST/ACS and HST/WFC3

imaging from CANDELS (Grogin et al. 2011; Koekemoer et al. 2011). We thus assemble the most complete near-infrared photometry compilation available for EGS-z11-R0.

For the JWST/MIRI photometry of EGS-z11-R0, we used observations from the Cycle 2 GO 3794 *MIRI EGS Galaxies Active Galactic Nucleus* survey (MEGA, PI: A. Kirkpatrick; Backhaus et al. 2025), which provides imaging data in four broad-band filters from 7 to 21 μm (F770W, F1000W, F1500W, F2100W). The mosaics have been reduced and calibrated with the Rainbow pipeline (Pablo G. Pérez-González, private communication). We then performed template-fitting photometry using τ -PHOT v2.0 (Merlin et al. 2016) synthetic NIRCcam and MIRI PSFs generated with STPSF (Perrin et al. 2014). In addition, to make the flux uncertainties consistent with the dispersion of fluxes, we selected different magnitude bins and we injected 500 artificial sources of such flux, whose photometry was computed using τ -PHOT. We computed the ratio between the standard deviation of the measured fluxes and the median uncertainty for each bin and extrapolated the rescaling factor as a function of the injected magnitude with a second-degree polynomial. We finally rescaled EGS-z11-R0 flux uncertainties by a multiplicative factor derived from the aforementioned function based on its photometry. The overall MIRI catalog will be presented in Catone et al. (in prep.).

The multiwavelength cutouts are shown in Fig. 3, with the corresponding flux measurements in all the considered bands reported in Table 2. The MSA/NIRSspec layout of the PRISM observation is illustrated in the RGB NIRCcam cutout of EGS-z11-R0, as depicted in Figure 4.

2.3. Morphology

We characterized EGS-z11-R0’s morphology in all JWST/NIRCcam detection bands (F277W, F356W, F410M, F444W) using GALFIT (Peng et al. 2002). We tested two scenarios — fitting a pure PSF model (generating empirical PSFs via the STPSF package in each band) and a PSF plus an extended Sérsic component. A pure-PSF fit yields $\chi^2_{\text{red}} = 0.092$ – 0.135 with smooth residuals in all bands, while the addition of an extended component does not appreciably improve our fits ($\Delta\chi^2 < 0.002$). We therefore conclude that the source is consistent with being unresolved in all detection bands. We derive an upper limit on its effective radius at $z = 11.452$ by taking half of the tabulated STScI empirical FWHM of the detection bands. The F277W band has the smallest FWHM ($0.092''$), yielding a physical size upper limit of 177.8 pc. The F444W band, which has the largest FWHM among the detection bands ($0.145''$), yields a physical upper limit of 280.1 pc.

3. UV slope measurements

Figure 5 places EGS-z11-R0 in the $M_{\text{UV}}-\beta_{\text{UV}}$ plane at $10 \lesssim z \lesssim 12$, together with recent photometric and spectroscopic measurements from the literature (Cullen et al. 2023, 2024; Austin et al. 2025; Casey et al. 2024; Asada et al. 2026; Mitsuhashi et al. 2025). The dashed relations represent the best-fit $\beta_{\text{UV}}-M_{\text{UV}}$ trends derived by Cullen et al. (2024) in the redshift intervals $10 < z < 11$ and $11 < z < 12$.

While the majority of galaxies at these epochs exhibit very blue rest-frame UV slopes ($\beta_{\text{UV}} \lesssim -2$), consistent with dust-poor and metal-poor stellar populations, EGS-z11-R0 lies significantly above the canonical relations, with $\beta_{\text{UV}} > -1.5$. In Sect. 2.1 we derived the UV slope β_{UV} from the NIRSspec spec-

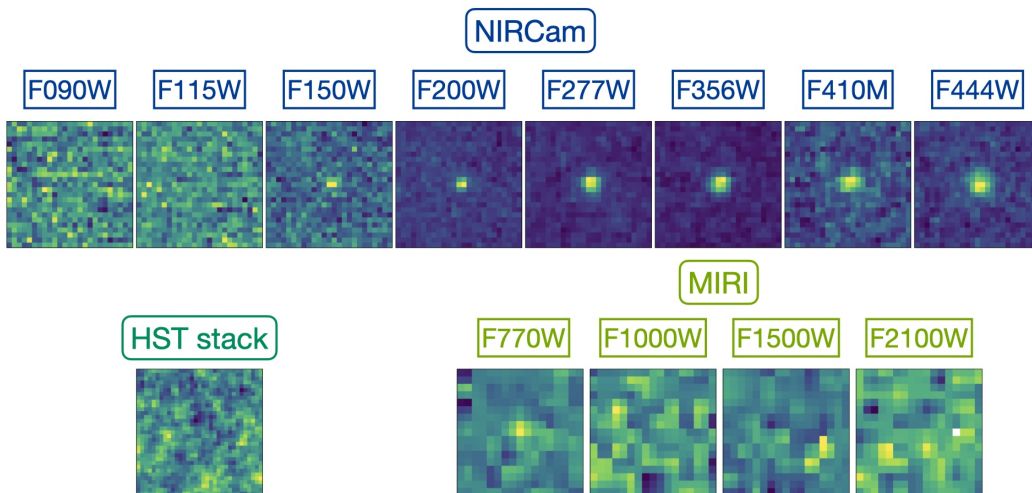


Fig. 3. Multiwavelength photometric cutouts of EGS-z11-R0: NIRCam bands (upper row, from DJA mosaics) and MIRI (bottom right row). For HST, we report the stacked frame of all the available bands (bottom left), confirming the dropout nature of the source. Each image has a size of $1'' \times 1''$.

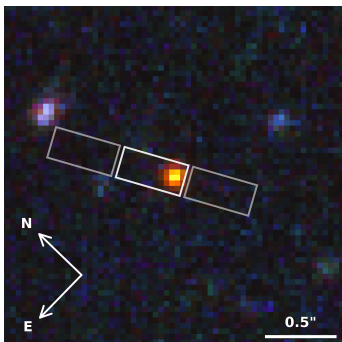


Fig. 4. RGB NIRCam image of EGS-z11-R0. The gray boxes show the MSA shutters of the NIRSpec/PRISM observation. The stamp has a size of $2.5'' \times 2.5''$ and it is oriented as indicated by the arrows. The image was created using Trilog⁴ and GIMP v 3.0.8⁵ by assigning the F090W, F115W filters to the B channel, F150W, F200W, and F277W to the G channel and F356W, F410M, and F444W to the R channel.

trum. As an independent check, we applied the same methodology to the NIRCam photometry. Interpolating the broadband fluxes over the same rest-frame wavelength range yields $\beta_{UV} = -1.20 \pm 0.28$. This value is fully consistent with the spectroscopic estimate, although slightly bluer, and still places the source among galaxies with red UV continua. For clarity, Fig. 5 shows both determinations of β_{UV} , illustrating the uncertainty associated with the slope measurement.

Its location overlaps with the subset of “red” $z \sim 12$ photometric candidates identified by Mitsuhashi et al. (2025), highlighted in Figure 5 with orange starred symbols. These objects deviate markedly from the typical $M_{UV} - \beta_{UV}$ scaling relations and represent a rare population of red UV-continuum sources at cosmic dawn. As discussed by Mitsuhashi et al. (2025), such red slopes at $z > 10$ cannot be easily explained by stellar population age or metallicity alone, given the short age of the Universe (~ 350 Myr at $z \sim 12$). Instead, two main physical mechanisms have been proposed: (i) significant dust attenuation or (ii) strong nebular continuum emission powered by extremely hot, massive stars embedded in dense gas (Katz et al. 2025).

In the dust-reddening scenario, values of $A_V \sim 0.5 - 1$ mag are required to reproduce $\beta_{UV} \gtrsim -1.5$ (Mitsuhashi et al. 2025). Such extinction levels are substantially higher than the median

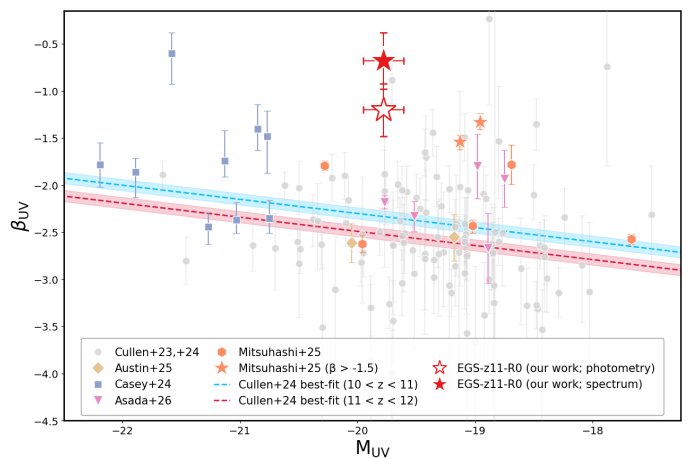


Fig. 5. UV continuum slope β_{UV} as a function of absolute UV magnitude M_{UV} at $z \sim 10-12$. Gray circles show literature measurements from Cullen et al. (2023, 2024), while colored symbols denote individual sources from Casey et al. (2024); Austin et al. (2025); Asada et al. (2026), and Mitsuhashi et al. (2025). Star symbols highlight the subset of Mitsuhashi et al. (2025) sources with $\beta_{UV} > -1.5$ and EGS-z11-R0 (this work; filled red star for the β_{UV} from spectroscopy and empty red star for the β_{UV} from the photometry alone). The dashed blue and red lines represent the best-fit $\beta_{UV} - M_{UV}$ relations from Cullen et al. (2024) for $10 < z < 11$ and $11 < z < 12$, respectively, with shaded regions indicating their associated uncertainties.

values inferred for the general $z > 10$ population, suggesting that these systems may represent a short-lived, obscured phase of rapid stellar mass assembly. In this framework, red monsters could be the dusty precursors of the so-called “blue monsters”, in which radiation-driven outflows have cleared the line of sight by displacing the dust and gas to distances much larger than the effective radius.

Alternatively, a nebular-continuum-dominated spectrum can also produce red UV slopes without invoking large dust masses. However, reproducing $\beta_{UV} > -1.5$ through nebular emission requires extreme physical conditions, including high gas densities ($n_H \gtrsim 10^4 \text{ cm}^{-3}$) and stellar effective temperatures $T_{\text{eff}} \gtrsim 5 \times 10^4$ K, as shown by the Cloudy modeling in Mitsuhashi et al. (2025). These parameters imply ionizing photon production efficiencies

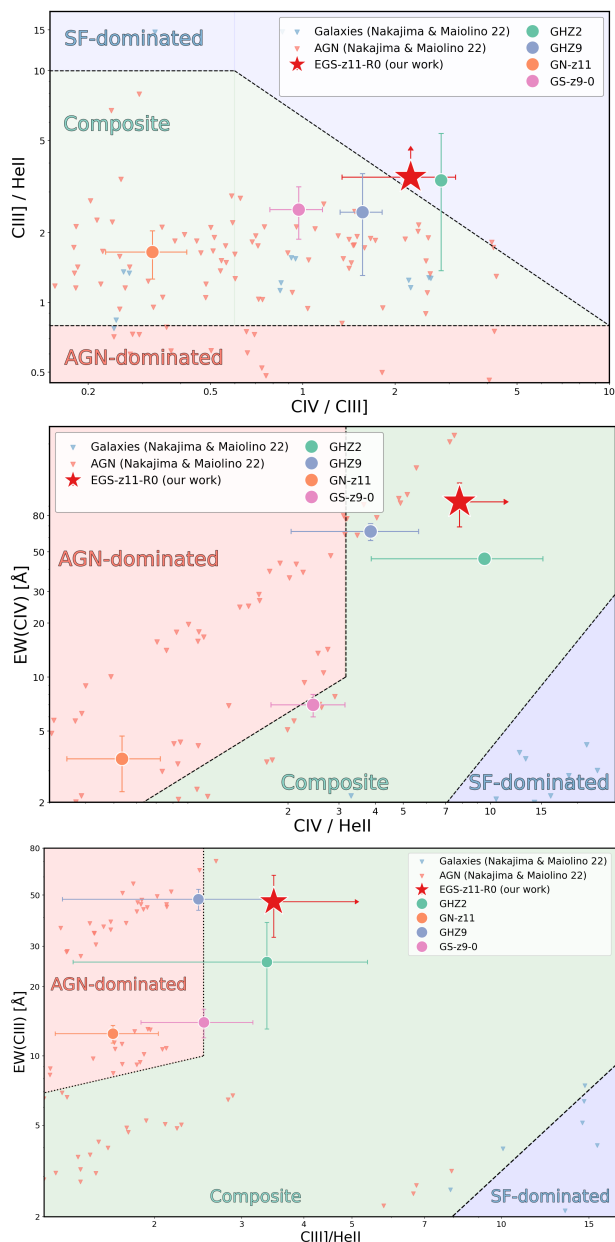


Fig. 6. Rest-frame UV diagnostic diagrams for EGS-z11-R0 and comparison with $z \geq 9$ galaxies. We also display AGN and SFG models from Nakajima & Maiolino (2022a) with $\log U$ and Z_{gas} consistent within 1σ with the CIGALE best-fit estimates of EGS-z11-R0 as red and blue triangles respectively. **Top panel:** $C\text{IV}/C\text{III]}$ versus $C\text{III]}/\text{HeII}$ line ratios, with dashed curves indicating the approximate boundaries between AGN-dominated (red shaded area), composite (green shaded area), and star-formation (SF)-dominated ionizing sources (blue shaded area). **Middle panel:** $\text{EW}(C\text{IV})$ as a function of $C\text{IV}/\text{HeII}$. **Bottom panel:** $\text{EW}(C\text{III]})$ versus $C\text{III]}/\text{HeII}$. The red star marks EGS-z11-R0 (this work), while colored symbols denote GHZ2, GN-z11, GHZ9, and GS-z9-0. Error bars represent 1σ uncertainties. The position of EGS-z11-R0 in these diagnostic planes is consistent with a hard ionizing spectrum in the composite/SF-dominated regime.

significantly above those of standard stellar populations, potentially pointing toward very massive stars or metal-poor starbursts. We will further discuss these possible scenarios in the next sections.

⁴ <https://github.com/dancoe/Trilogy>

⁵ <https://www.gimp.org>

Table 2. Photometric estimates and 1σ uncertainties in the available HST and JWST bands for EGS-z11-R0.

Instrument	Band	Photometry [nJy]
HST/ACS	F435W	-1.74 ± 3.56
HST/ACS	F606W	-0.11 ± 3.12
HST/ACS	F775W	–
HST/ACS	F814W	-4.94 ± 3.99
HST/WFC3	F105W	–
HST/WFC3	F125W	12.13 ± 4.54
HST/WFC3	F140W	13.15 ± 6.96
HST/WFC3	F160W	7.99 ± 4.17
JWST/NIRCam	F090W	0.25 ± 3.91
JWST/NIRCam	F115W	8.76 ± 5.25
JWST/NIRCam	F150W	11.30 ± 5.25
JWST/NIRCam	F200W	22.86 ± 4.92
JWST/NIRCam	F277W	27.98 ± 2.08
JWST/NIRCam	F356W	31.88 ± 2.36
JWST/NIRCam	F410M	25.86 ± 3.76
JWST/NIRCam	F444W	36.53 ± 3.07
JWST/MIRI	F770W	106.12 ± 27.79
JWST/MIRI	F1000W	55.53 ± 58.99
JWST/MIRI	F1500W	-335.67 ± 190.56
JWST/MIRI	F2100W	-756.08 ± 548.76

4. Emission lines: AGN vs. star formation

The detection of multiple rest-frame UV emission lines in the NIRSPEC spectrum of EGS-z11-R0 allows us to investigate the nature of its ionizing source. In Figure 6 we place EGS-z11 (red star) in a set of UV diagnostic diagrams commonly used to distinguish among AGN-dominated, SF-dominated, and composite ionizing spectra. We compare line ratios and equivalent widths (EW) with other spectroscopically confirmed sources at $z \geq 9$ (e.g., GN-z11, GHZ2, GHZ9, GS-z9-0, Bunker et al. 2023; Maiolino et al. 2024; Castellano et al. 2024; Curti et al. 2025), following an approach similar to that adopted by Napolitano et al. (2025b) for GHZ9.

In the top panel of Figure 6 we show the $C\text{IV}/C\text{III]}$ versus $C\text{III]}/\text{HeII}$ diagram. These ratios are sensitive to both the hardness of the ionizing radiation field and the ionization parameter. The dashed demarcation curves indicate the approximate separation between AGN-dominated, composite, and SF-dominated regimes, calibrated using photoionization models (e.g., Feltre et al. 2016; Gutkin et al. 2016; Hirschmann et al. 2019; Nakajima & Maiolino 2022b). EGS-z11-R0 lies in the composite region, consistent within the uncertainties with both AGN and extreme stellar ionizing spectra. This degeneracy mirrors what has been reported for other $z > 10$ systems (e.g., GN-z11 and GHZ9), where UV line-ratio diagnostics alone do not provide a unique classification.

The middle and bottom panels of Figure 6 explore EW-based diagnostics, namely $\text{EW}(C\text{IV})$ versus $C\text{IV}/\text{HeII}$ and $\text{EW}(C\text{III]})$ versus $C\text{III]}/\text{HeII}$. As discussed by Napolitano et al. (2025b), the combination of large EWs ($\gtrsim 30\text{--}50\text{ \AA}$) and elevated metal-to-HeII ratios generally requires a hard ionizing spectrum. In EGS-z11, the observed EWs are significantly larger than typically expected for standard stellar populations at sub-solar metallicity, placing the source toward the upper envelope of the SF-dominated models and overlapping with the composite region. Pure stellar photoionization models can reproduce such high

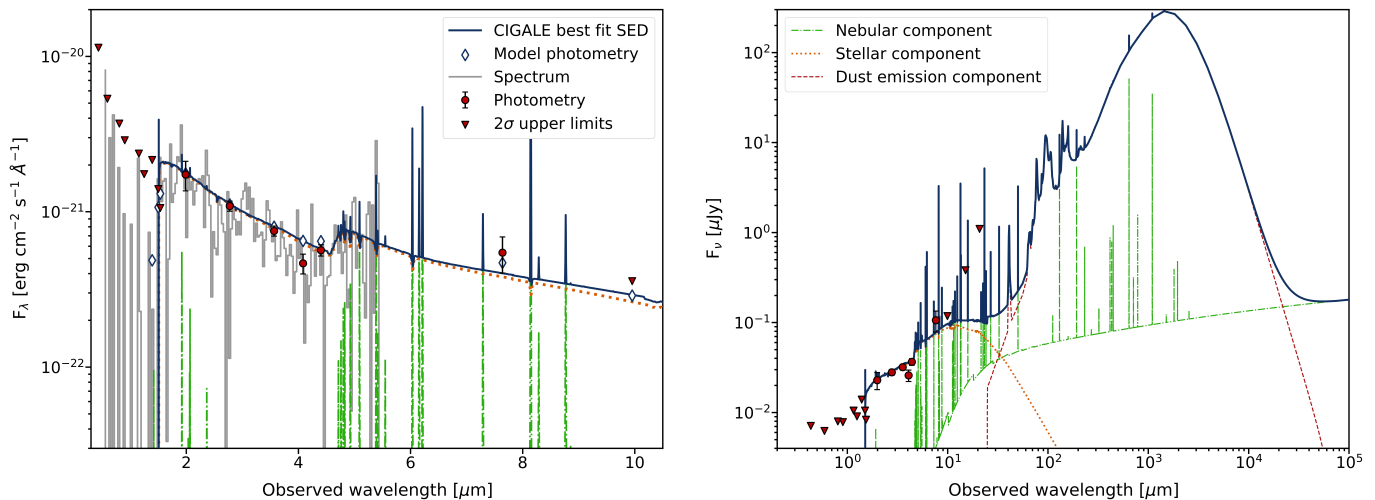


Fig. 7. Best fit Spectral Energy Distribution (SED) modeling of EGS-z11-R0 with CIGALE. **Left panel:** Observed *NIRSpec/PRISM* spectrum rebinned with a bin size of $\Delta\lambda = 3\mu\text{m}$ (gray), overlaid with the best-fit CIGALE model (solid blue line). Blue diamonds indicate the model photometry integrated over the observed bands, red circles show the measured photometric fluxes, and red triangles denote 2σ upper limits. The stellar continuum is marked as an orange dotted line. The green dash-dotted curve highlights the contribution from nebular emission lines. **Right panel:** Full best-fit SED extended to far-infrared wavelengths, decomposed into stellar (orange dotted), nebular (green dash-dotted), and dust emission (red dashed) components. The solid blue curve shows the total model flux density.

EWs only under extreme conditions, including very low metallicity and high ionization parameter ($\log U \gtrsim -2$), while AGN models naturally predict strong high-ionization features.

However, unlike the case of GHZ9 (Napolitano et al. 2025b), EGS-z11-R0 does not show unambiguous signatures of a dominant AGN, such as extremely high-ionization lines (e.g., [He II], [Ne III]) or rest-frame optical ratios firmly located in the AGN regime. Instead, its position in the diagnostic planes is consistent with a hard composite spectrum, potentially arising from a combination of intense star formation and a moderate AGN contribution.

The emission-line diagnostics presented in Figure 6 suggest that EGS-z11-R0 hosts a hard ionizing radiation field, but they do not uniquely require an AGN-dominated scenario. This interpretation is consistent with our SED modeling (Section 5), which favors a composite solution with a non-negligible AGN fraction while still requiring significant dust attenuation to reproduce the red UV slope. In this framework, EGS-z11-R0 may represent a transitional “red monster” system in which rapid stellar mass assembly, dust enrichment, and possible early black-hole growth occur concurrently.

5. SED fitting: physical parameters

To constrain the physical properties of EGS-z11, we performed spectral energy distribution (SED) fitting using the available HST, JWST/NIRCam, and JWST/MIRI photometry listed in Table 1 and the *NIRSpec* spectrum. The best-fit solution is shown in Figure 5, where the observed spectrum and photometric data points are compared to the composite model.

We modeled the SED using CIGALE (Burgarella et al. 2025), adopting a flexible star-formation history (SFH) (Carvajal-Bohorquez et al. 2025) and including both stellar (Bruzual & Charlot 2003) and nebular emission (Inoue 2011; Ferland et al. 1998, 2013) components. We assumed a Chabrier (2003) initial mass function and explored sub-solar metallicities, consistent with the spectroscopic constraints. Dust attenuation was modeled using a Calzetti et al. (2000)-like law, allowing for a range

of A_V values. In addition, we included an AGN component parameterized by its fractional contribution to the total infrared luminosity (f_{AGN}). For the AGN component, we include both the *dale2014* (Dale et al. 2014) and *fritz2006* (Fritz et al. 2006) models. We summarize our SED-fitting set-up and we report the adopted prior grids in Table 3.

The left panel of Figure 5 shows the best-fit model overlaid on the *NIRSpec* spectrum. The model successfully reproduces the red UV continuum slope, the continuum normalization, and the overall optical-to-mid-IR flux ratios. The right panel displays the full SED decomposition, separating the stellar, nebular, and dust components. The nebular contribution (dash-dotted curve) is non-negligible in the rest-frame UV and optical, but does not dominate the continuum shape.

The best-fit solution favors a stellar mass of $\log(M_*/M_\odot) \sim 8.5\text{--}9.0$, depending on the assumed AGN fraction (see also Figure 7), placing EGS-z11 among the most massive known galaxies at $z > 11$. The inferred star-formation rate is of order $\text{SFR} \sim 10\text{--}30 M_\odot \text{yr}^{-1}$, consistent with rapid stellar mass assembly within the first few hundred Myr of cosmic time. The SFH (Figure 8) indicates a sustained or rising star-formation episode rather than a short, instantaneous burst.

Importantly, the fit requires non-negligible dust attenuation to reproduce the observed UV slope. The preferred value is $A_V \sim 0.5\text{--}1.0$ mag, significantly higher than typical values measured for the bulk of $z > 10$ galaxies. Models with negligible dust fail to simultaneously match the UV continuum and the longer-wavelength NIRCam/MIRI photometry. In addition, the best-fit solution predicts a dust luminosity of $L_{\text{IR}} = (4.80 \pm 1.20) \times 10^{11} L_\odot$. These results support the interpretation that EGS-z11-R0 is undergoing an obscured phase of star formation, consistent with the “red monster” scenario discussed in previous sections.

5.1. AGN dependence

Figure 9 illustrates the impact of fixing the AGN fraction (f_{AGN}) to progressively higher values in our CIGALE modeling, while Table 4 summarizes the corresponding best-fit physical param-

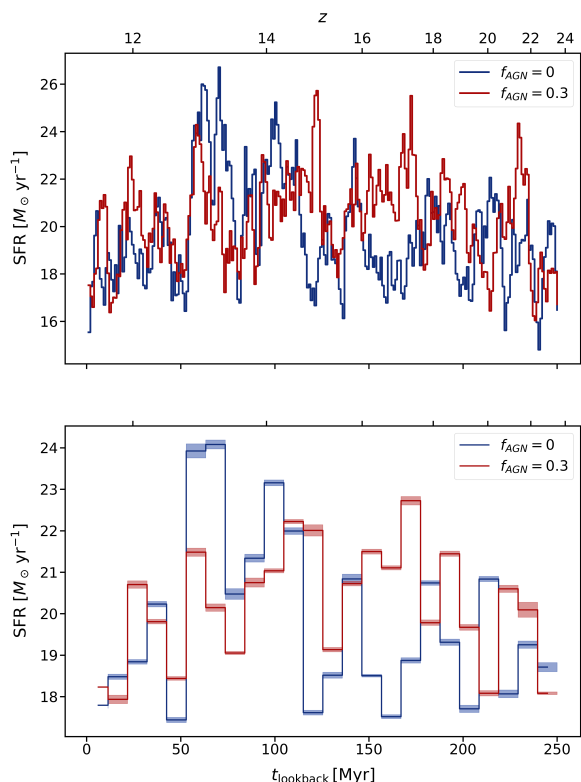


Fig. 8. Star formation histories (SFHs) derived from the CIGALE modeling of EGS-z11-R0. The blue curve shows the stochastic SFH corresponding to the best-fit solution presented in Figure 7, where no AGN contribution is required. The red curve represents the SFH obtained when forcing an AGN fraction of $f_{\text{AGN}} = 0.3$ using the `fritz2006` module (see Table 4). Top panel: instantaneous stochastic SFHs. Bottom panel: same SFHs smoothed over a 10 Myr timescale (solid lines) and its associated bin error (shaded regions), computed as the standard error of the mean. It is worth noting that in Table 4 the value reported for each physical parameters are referred to the Bayesian analysis of CIGALE, turning into potential offset with the values of the best fit (as this SF history).

ters for the different configurations. Although the open-prior solution presented in Section 5 does not require a dominant AGN component, the emission-line diagnostics (Figure 6) allow for a composite stellar+AGN scenario. We therefore explored forced solutions with $f_{\text{AGN}} = 0.3$ and $f_{\text{AGN}} = 0.6$ to assess how increasing AGN contributions modify the inferred SED and physical parameters. To this aim, as anticipated at the beginning of this Section, we tested two different AGN prescriptions available in CIGALE: the torus-based models of Fritz et al. (2006), shown in the left panel of Fig. 9, and the empirical infrared templates of Dale et al. (2014), shown in the right panel. We note that the AGN fraction has different definitions in the two considered models⁶.

When forcing $f_{\text{AGN}} = 0.6$, in both cases the best-fit is in tension with the observational constraints: the model of Fritz exceeds the upper limits in the MIRI/F1000W band, while the Dale model outshines the UV range. In general, the redistribution of bolometric luminosity toward the AGN component suppresses the stellar and dust-reprocessed emission required to match the broadband photometry. We also tested the outcome of an extreme case with $f_{\text{AGN}} = 1$ (AGN only without galaxy). Although this solution could still reproduce the UV, it largely fails in re-

covering the MIRI F770W, underestimating the optical continuum emission. In contrast, the $f_{\text{AGN}} = 0.3$ solution remains broadly consistent with the observed photometry and spectrum. The models reproduce the NIRCам data without violating the MIRI upper limits. The overall SED shape remains similar to the open-prior best-fit, indicating that a moderate AGN fraction does not significantly distort the continuum balance.

The impact of these configurations on the inferred physical parameters is summarized in Table 4. Increasing the AGN fraction systematically reduces the stellar mass and star-formation rate, as part of the total luminosity is attributed to the AGN component rather than to stars. For the `dale2014` run, the stellar mass decreases from $\log(M_{\star}/M_{\odot}) = 9.64 \pm 0.13$ (open prior) to 9.20 ± 0.14 for $f_{\text{AGN}} = 0.3$, and further down to 8.64 ± 0.32 for $f_{\text{AGN}} = 0.6$. This corresponds to nearly an order-of-magnitude suppression of M_{\star} in the high-AGN case. A similar trend is observed for the SFR, which drops from $\sim 42 M_{\odot} \text{ yr}^{-1}$ to ~ 9.6 and $\sim 3.9 M_{\odot} \text{ yr}^{-1}$ for $f_{\text{AGN}} = 0.3$ and 0.6 , respectively.

A comparable behavior is seen when adopting the `fritz2006` AGN module: while $f_{\text{AGN}} = 0.3$ yields stellar masses $\log(M_{\star}/M_{\odot}) \sim 9.5$ and SFRs of $\sim 30 M_{\odot} \text{ yr}^{-1}$, increasing the AGN fraction to 0.6 again lowers the stellar mass and SFR. Importantly, even in the AGN-inclusive runs, substantial stellar reddening ($E(B - V)_{\star} \sim 0.25 - 0.3$) is still required, indicating that dust attenuation remains necessary to reproduce the red UV slope.

Overall, these tests demonstrate that while a moderate AGN fraction ($\sim 30\%$, in the dust component) is fully compatible with both the broadband SED and the composite nature suggested by the UV line diagnostics, a dominant AGN contribution ($\geq 60\%$) is disfavored by the data. The red UV slope and mid-infrared flux of EGS-z11-R0 are more naturally explained by a dust-enriched stellar population, possibly accompanied by a secondary AGN component, rather than by an AGN-dominated energy budget.

5.2. Comparison to literature high- z red sources

In a quantitative comparison with other recently reported $z > 10$ systems with red UV slopes, the physical properties of EGS-z11-R0 closely match the photometric dust-enriched population identified by Mitsuhashi et al. (2025). Those authors show that reproducing $\beta_{\text{UV}} \gtrsim -1.5$ requires dust attenuation of $A_V \sim 0.5 - 1$ mag, stellar masses $\log(M_{\star}/M_{\odot}) \sim 8 - 9$, and ionization parameters $\log U \sim -2$ to -1.5 . Our best-fit solution yields $A_V \sim 1.0 - 1.3$, $\log(M_{\star}/M_{\odot}) \sim 8.6 - 8.9$, and similarly elevated ionization conditions, placing EGS-z11-R0 fully within the same parameter space. In addition, the large rest-frame equivalent widths observed for high-ionization UV lines are consistent with the extreme nebular conditions inferred by Mitsuhashi et al. (2025), although our SED modeling indicates that dust attenuation remains the primary driver of the red UV slope.

Compared to GHZ9 at $z = 10.145$ studied by Napolitano et al. (2025b), several similarities and differences emerge. GHZ9 has a stellar mass of $M_{\star} \sim (3 - 7) \times 10^8 M_{\odot}$ and nebular reddening $E(B - V) \sim 0.3$ (corresponding to $A_V \sim 1$ for a Calzetti law), comparable to the values derived here. Its ionization parameter ($\log U \sim -1.9$ to -1.6) and extreme UV EWs (e.g., $\text{EW}(\text{C IV}) \sim 65 \text{ \AA}$, $\text{EW}(\text{C III}) \sim 48 \text{ \AA}$) require a very hard radiation field and are accompanied by an X-ray detection implying a black-hole mass of order $10^8 M_{\odot}$. In contrast, while EGS-z11-R0 shows similarly elevated EWs and attenuation (but larger stellar mass), we lack independent AGN tracers such as X-ray

⁶ $f_{\text{AGN}}(\text{Dale}) = L_{\text{AGN}}/L_{\text{dust}}$; $f_{\text{AGN}}(\text{Fritz}) = L_{\text{AGN}}/(L_{\text{AGN}} + L_{\text{dust}})$

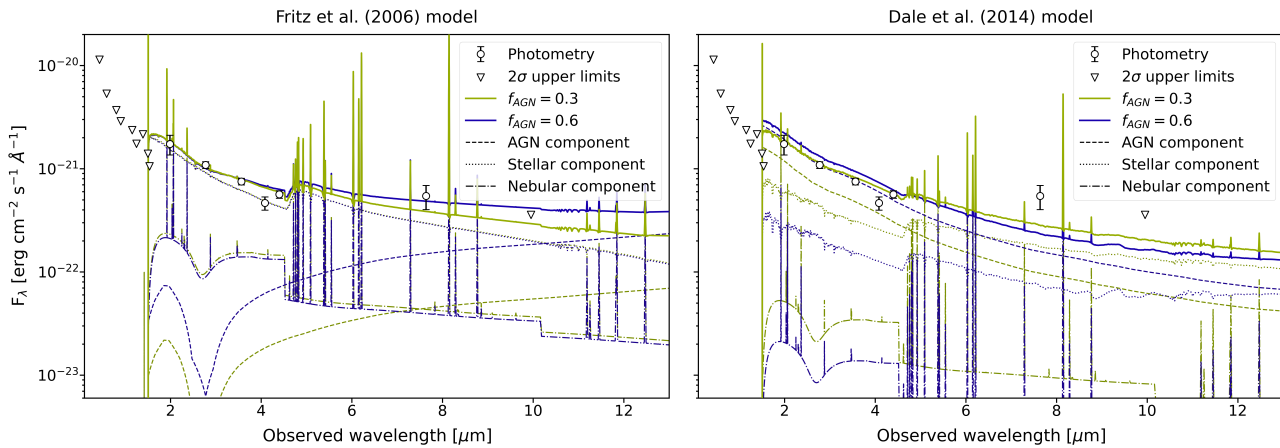


Fig. 9. Same as Fig. 7, but showing CIGALE SED models where the AGN fraction is fixed to different values ($f_{\text{AGN}} = 0.3$ and $f_{\text{AGN}} = 0.6$). The observed photometry (circles) and 2σ upper limits (triangles) are compared with the total composite models (solid curves), while the individual AGN (dashed), stellar (dotted), and nebular (dash-dotted) components are shown separately to illustrate the impact of varying the AGN contribution on the overall SED shape. Left panel: best-fit SEDs with AGN component modeled using the `fritz2006` module. Right panel: best-fit SEDs with AGN component modeled using the `dale2014` module.

emission, and our line-ratio diagnostics remain consistent with a composite or extreme star-forming solution.

This comparison suggests that EGS-z11-R0 may occupy a similar region of parameter space as GHZ9 in terms of stellar mass, ionization state, and dust content, but with a less dominant or more obscured AGN contribution. In the framework proposed for “red monsters”, EGS-z11-R0 could represent either a dust-enshrouded phase preceding efficient AGN feedback or a system in which intense star formation alone is capable of producing the observed hard ionizing spectrum.

Overall, the best-fit SED solution points toward a compact, massive, dust-enriched galaxy at $z \sim 11.5$, possibly hosting a moderate AGN contribution during a phase of rapid early assembly.

6. Discussion

6.1. Early dust and the emergence of red monsters at $z > 10$

The spectroscopic confirmation of EGS-z11-R0 demonstrates that dust-enriched galaxies already existed at $z \simeq 11.5$, only ~ 400 Myr after the Big Bang. Its red UV slope ($\beta_{\text{UV}} \sim -1$) and the dust attenuation required by our SED modeling ($A_V \sim 1$ mag) place the system well above the canonical $M_{\text{UV}}-\beta_{\text{UV}}$ relation followed by the majority of $z > 10$ galaxies, which typically exhibit very blue continua consistent with dust-poor stellar populations. Together with other recently reported candidates (e.g., Mitsuhashi et al. 2025; Donnan et al. 2025), EGS-z11-R0 strengthens the emerging picture that a population of dust-reddened galaxies may already be present at cosmic dawn.

This result carries important implications for the origin of dust in the early Universe. Several recent theoretical models predict that the bulk of dust mass growth in galaxies occurs through grain growth in the interstellar medium rather than through direct stellar production. In these models, efficient dust enrichment requires the ISM to reach sufficiently high metallicities and densities, implying a delayed rise of the dust content during the first stages of galaxy evolution (e.g. Narayanan et al. 2025). As a consequence, such frameworks generally predict that heavily obscured galaxies should be extremely rare, or absent, at $z \gtrsim 10$.

The discovery of EGS-z11, together with the dusty candidate reported by Donnan et al. (2025), challenges this expectation.

An alternative interpretation involves the geometry and dynamical state of the dusty interstellar medium. In the framework proposed by Ferrara (2024), early galaxies may experience a short-lived “red monster” phase during which rapid star formation proceeds within a dust-enshrouded environment. During this stage, radiation pressure builds up and eventually drives powerful outflows that expel gas and dust from the central regions, revealing the young stellar population and producing the UV-bright “blue monsters” commonly observed at $z > 10$.

Several observational properties of EGS-z11-R0 are consistent with this scenario. First, the significant dust attenuation inferred from the SED modeling indicates that the galaxy is observed during a heavily obscured phase of its evolution. Second, the star-formation histories derived from the CIGALE modeling (Fig. 8) show a rising or approximately constant star-formation rate rather than a rapidly declining burst. This behavior is remarkably consistent with the predictions of the feedback-regulated model of Ferrara (2024), in which the dust-obscured phase is characterized by sustained star formation lasting a substantial fraction of the galaxy lifetime. In this framework, a large fraction of the stellar mass is assembled during the obscured stage before radiation-driven outflows disperse the dust and transition the system into the UV-bright phase.

These results imply that the earliest galaxies may undergo phases of substantial dust obscuration much earlier than predicted by models in which dust growth is primarily regulated by slow ISM processes. If systems such as EGS-z11-R0 represent a common stage of early galaxy evolution, a non-negligible fraction of star formation at $z > 10$ may occur in dusty environments that remain difficult to detect through rest-frame UV surveys alone.

6.2. Possible AGN contribution and implications for early black-hole seeds

While the broadband SED and UV line diagnostics are broadly consistent with a star-forming system, the presence of a composite stellar+AGN spectrum remains a viable possibility for EGS-z11-R0 (Sect. 5.1). If part of the observed UV continuum originates from accretion onto a central black hole, the required black-hole mass can be estimated from the observed rest-frame

Table 3. Prior grids for free parameters used in our CIGALE SED-fitting runs.

CIGALE parameter	Grid values	Description
Stochastic SFH [sfh_stochasticity_physgaussproc]		
Age _{main}	10, 100, 250, 500	Age of the main population in Myr
Baseline code	1	Baseline SFH (1: constant)
σ_{reg}	0.70	Amplitude for regulator PSD (nat-log)
σ_{dyn}	0.34	Amplitude for GMC/dynamical PSD (nat-log)
τ_{inflow}	100, 120, 140	Inflow correlation timescale in Myr
τ_{eq}	15	Equilibrium/depletion timescale in Myr
τ_{GMC}	5	GMC/dynamical timescale in Myr
$T_{\text{burst, short}}$	10, 50	Short-timescale averaging window for burstiness metrics in Myr
$T_{\text{burst, long}}$	100, 500	Long-timescale averaging window for burstiness metrics in Myr
$T_{\text{burst, cut}}$	30, 50	Cutoff timescale for high-frequency power fraction in Myr
SSP [bc03]		
Z	0.0001, 0.02, 0.05	Stellar metallicity
Nebular [nebular]		
$\log(U)$	-4.0, -3.0, -2.0, -1.0	Ionisation parameter
Z_{gas}	0.0001, 0.02, 0.051	Gas metallicity
N_e	100, 1000	Electron density
Dust attenuation [dustatt_modified_starburst]		
E(B-V) _{lines}	0.01, 0.1, 0.25, 0.5, 0.75, 1, 1.5, 2, 2.5, 3	Color excess of the nebular lines light
E(B-V) _{factor}	0.44, 1	Reduction factor to compute the stellar continuum attenuation
R_V	4.05	$A_V / E(B-V)$ (Calzetti law)
Dust emission [dale2014]		
f_{AGN}	0.0, 0.1, 0.5, 0.9	AGN fraction
α	2, 3	Alpha slope
Dust emission [dl2014] [†]		
α	2, 3	Powerlaw slope $dU/dM \propto U^\alpha$
AGN [fritz2006] [†]		
ψ	30.1, 70.1	Angle between equatorial axis and line of sight
f_{AGN}	0.3, 0.6	AGN fraction
$\lambda_{f_{\text{AGN}}}$	0/0	Wavelength range in microns where to compute the AGN fraction (0/0: total dust luminosity)
E(B-V)	0.03, 0.1, 0.3, 0.5	E(B-V) for the extinction in the polar direction in magnitudes

Notes. †: These modules were used in place of dale2014.

UV flux. Adopting the observed continuum level and assuming that the AGN radiates at the Eddington limit, the corresponding black-hole mass required to reproduce the observed UV emission would be on the order of $M_{\text{BH}} \simeq 3 \times 10^5 M_\odot$ (in the case of an AGN contribution $f_{\text{AGN}} = 0.6$). Such a mass scale is particularly intriguing in the context of early black-hole seed formation. Black holes with masses of $\sim 10^5 M_\odot$ fall within the range expected for massive seed channels such as direct-collapse black holes (DCBHs), as well as for primordial black holes (PBHs) that may have formed in the early Universe. In particular, recent work by Matteri et al. (2025) has explored scenarios in which a population of PBHs with characteristic masses of $\sim 10^4$ – $10^5 M_\odot$ contributes to the UV luminosity of super-early galaxies through accretion-powered emission. In these models, even a small fraction of halos hosting accreting PBHs can significantly boost the UV luminosity of high-redshift galaxies and help reproduce the observed luminosity function at $z \gtrsim 10$.

Within this framework, a system such as EGS-z11-R0 could naturally host an accreting black hole contributing a fraction of the observed UV continuum.

In the context of the radiative-feedback model of Ferrara (2024), the possible presence of an accreting black hole may also be connected to the “red monster” phase of galaxy evolution. If a central black hole is already present during this stage, its accretion luminosity could contribute to the hard ionizing radiation field and to the observed UV continuum. In this interpretation, EGS-z11-R0 may represent a system caught during the early obscured growth phase in which both rapid star formation and black-hole accretion are simultaneously building the stellar and black-hole mass of the galaxy.

Table 4. Physical parameters of EGS-z11-R0 determined by CIGALE Bayesian analysis with different AGN configurations.

Parameter	dale2014			fritz2006	
	$f_{AGN} \approx 0^*$	$f_{AGN} = 0.3$	$f_{AGN} = 0.6$	$f_{AGN} = 0.3$	$f_{AGN} = 0.6$
$\log(M_*/M_\odot)$	9.64 ± 0.13	9.20 ± 0.14	8.64 ± 0.32	9.48 ± 0.18	9.29 ± 0.39
SFR [$M_\odot \text{ yr}^{-1}$]	42.05 ± 14.52	9.64 ± 1.67	3.86 ± 0.76	30.17 ± 16.07	14.64 ± 5.49
E(B-V) _* [mag]	0.33 ± 0.03	0.29 ± 0.09	0.41 ± 0.43	0.28 ± 0.08	0.25 ± 0.24
E(B-V) _{AGN} [mag]	–	–	–	0.32 ± 0.17	0.29 ± 0.17
E(B-V) _{neb} [mag]	0.73 ± 0.12	0.50 ± 0.29	0.65 ± 0.56	0.58 ± 0.19	0.48 ± 0.31

Notes. *: the physical parameters of this configuration are referred to the run with open priors.

7. Summary and Conclusions

We report the spectroscopic confirmation of EGS-z11-R0 at $z = 11.452 \pm 0.021$ using JWST/NIRSpec observations of the CEERS field. Our main results can be summarized as follows:

- The UV slope of EGS-z11-R0 places it well above the canonical $M_{UV} - \beta_{UV}$ relation followed by the majority of galaxies at $z > 10$, which typically exhibit very blue, dust-poor continua. The required attenuation ($A_V \sim 1$ mag) demonstrates that significant dust reservoirs were already present only ~ 400 Myr after the Big Bang.
- SED modeling combining spectroscopy with HST, NIRCам, and MIRI photometry yields a stellar mass $\log(M_*/M_\odot) \sim 9.2 - 9.6$ and a star-formation rate of $\sim 10 - 40 M_\odot \text{ yr}^{-1}$. The inferred star-formation history is rising or approximately constant, indicating sustained stellar mass growth rather than a short-lived burst.
- The significant dust attenuation, compact morphology, and rising star-formation history are consistent with the radiative-feedback scenario proposed by Ferrara (2024) in which early galaxies undergo a short-lived dust-obscured “red monster” phase during which a large fraction of their stellar mass forms before radiation-driven outflows disperse the dust and reveal the UV-bright system.
- Although the data do not require a dominant AGN component, the emission-line diagnostics and SED modeling remain compatible with a composite stellar+AGN spectrum. If part of the UV emission arises from Eddington-limited accretion, the implied black-hole mass would be $M_{BH} \sim 10^5 M_\odot$, a value intriguingly consistent with the expected mass range of massive early black-hole seeds such as direct-collapse black holes or primordial black holes.

Future JWST spectroscopy and deeper mid-infrared, sub-millimeter and radio observations will be crucial to establish the prevalence of these early dust-rich galaxies and to clarify their role in the earliest phases of galaxy and black-hole growth.

Acknowledgements. G.R., P.C., G.G. and A.G. are supported by the European Union – NextGeneration EU RFF M4C2 1.1 PRIN 2022 project 2022ZSL4BL INSIGHT. P.G.P.-G. acknowledges support from grant PID2022-139567NB-I00 funded by Spanish Ministerio de Ciencia, Innovación y Universidades MCIU/AEI/10.13039/501100011033, FEDER *Una manera de hacer Europa*. The authors thank the PI, Erica Nelson, and the team of the JWST GO proposal 4106 for making their data public. This work is based on one of the fillers of this program. We also thank Gabriel Brammer for spotting an error about the GRISM spectrum that we showed in the first version of this paper.

References

Asada, Y., Willott, C. J., Muzzin, A., et al. 2026, ApJ, 996, 115

- Astropy Collaboration, Robitaille, T. P., Tollerud, E. J., et al. 2013, A&A, 558, A33
- Austin, D., Adams, N., Conselice, C. J., et al. 2023, ApJ, 952, L7
- Austin, D., Conselice, C. J., Adams, N. J., et al. 2025, ApJ, 995, 43
- Backhaus, B. E., Kirkpatrick, A., Yang, G., et al. 2025, AJ, 170, 300
- Bagley, M. B., Finkelstein, S. L., Koekemoer, A. M., et al. 2023, ApJ, 946, L12
- Bruzual, G. & Charlot, S. 2003, MNRAS, 344, 1000
- Bunker, A. J., Saxena, A., Cameron, A. J., et al. 2023, A&A, 677, A88
- Burgarella, D., Buat, V., Theulé, P., et al. 2025, A&A, 699, A336
- Carvajal-Bohorquez, C., Ciesla, L., Laporte, N., et al. 2025, A&A, 704, A290
- Casey, C. M., Akins, H. B., Shuntov, M., et al. 2024, ApJ, 965, 98
- Castellano, M., Fontana, A., Treu, T., et al. 2023, ApJ, 948, L14
- Castellano, M., Napolitano, L., Fontana, A., et al. 2024, ApJ, 972, 143
- Chabrier, G. 2003, PASP, 115, 763
- Cox, I. G., Kartaltepe, J. S., Bagley, M. B., et al. 2025, arXiv e-prints, arXiv:2510.08743
- Cullen, F., McLeod, D. J., McLure, R. J., et al. 2024, MNRAS, 531, 997
- Cullen, F., McLure, R. J., McLeod, D. J., et al. 2023, MNRAS, 520, 14
- Curti, M., Witstok, J., Jakobsen, P., et al. 2025, A&A, 697, A89
- Dale, D. A., Helou, G., Magdis, G. E., et al. 2014, ApJ, 784, 83
- de Graaff, A., Brammer, G., Weibel, A., et al. 2025, A&A, 697, A189
- Dekel, A., Sarkar, K. C., Birnboim, Y., Mandelker, N., & Li, Z. 2023, MNRAS, 523, 3201
- Donnan, C. T., Dickinson, M., Taylor, A. J., et al. 2025, ApJ, 993, 224
- Feltre, A., Charlot, S., & Gutkin, J. 2016, MNRAS, 456, 3354
- Ferland, G. J., Korista, K. T., Verner, D. A., et al. 1998, PASP, 110, 761
- Ferland, G. J., Porter, R. L., van Hoof, P. A. M., et al. 2013, Rev. Mexicana Astron. Astrofis., 49, 137
- Ferrara, A. 2024, A&A, 684, A207
- Finkelstein, S. L., Bagley, M. B., Arrabal Haro, P., et al. 2025a, ApJ, 983, L4
- Finkelstein, S. L., Bagley, M. B., Arrabal Haro, P., et al. 2025b, ApJ, 983, L4
- Finkelstein, S. L., Leung, G. C. K., Bagley, M. B., et al. 2024, ApJ, 969, L2
- Foreman-Mackey, D., Hogg, D. W., Lang, D., & Goodman, J. 2013, PASP, 125, 306
- Fritz, J., Franceschini, A., & Hatziminaoglou, E. 2006, MNRAS, 366, 767
- Gandolfi, G., Rodighiero, G., Bisigello, L., et al. 2025, arXiv e-prints, arXiv:2502.02637
- Grogin, N. A., Kocevski, D. D., Faber, S. M., et al. 2011, ApJS, 197, 35
- Gutkin, J., Charlot, S., & Bruzual, G. 2016, MNRAS, 462, 1757
- Hainline, K. N., Shapley, A. E., Greene, J. E., & Steidel, C. C. 2011, ApJ, 733, 31
- Hainline, K. N., Shapley, A. E., Greene, J. E., et al. 2012, ApJ, 760, 74
- Harikane, Y., Inoue, A. K., Mawatari, K., et al. 2022, ApJ, 929, 1
- Heintz, K. E., Watson, D., Brammer, G., et al. 2024, Science, 384, 890
- Hirschmann, M., Charlot, S., Feltre, A., et al. 2019, MNRAS, 487, 333
- Inoue, A. K. 2011, MNRAS, 415, 2920
- Katz, H., Cameron, A. J., Saxena, A., et al. 2025, The Open Journal of Astrophysics, 8, 104
- Koekemoer, A. M., Faber, S. M., Ferguson, H. C., et al. 2011, ApJS, 197, 36
- Kokorev, V., Chávez Ortiz, Ó. A., Taylor, A. J., et al. 2025, ApJ, 988, L10
- Maiolino, R., Scholtz, J., Witstok, J., et al. 2024, Nature, 627, 59
- Marques-Chaves, R., Álvarez-Márquez, J., Colina, L., et al. 2026, arXiv e-prints, arXiv:2602.02322
- Matteri, A., Pallottini, A., & Ferrara, A. 2025, A&A, 697, A65
- Merlin, E., Bourne, N., Castellano, M., et al. 2016, A&A, 595, A97
- Merlin, E., Santini, P., Paris, D., et al. 2024, A&A, 691, A240
- Mitsuhashi, I., Suess, K. A., Leja, J., et al. 2025, arXiv e-prints, arXiv:2510.13240
- Morales, A. M., Finkelstein, S. L., Leung, G. C. K., et al. 2024, ApJ, 964, L24
- Naidu, R. P., Oesch, P. A., van Dokkum, P., et al. 2022, ApJ, 940, L14
- Nakajima, K. & Maiolino, R. 2022a, MNRAS, 513, 5134

- Nakajima, K. & Maiolino, R. 2022b, *MNRAS*, 513, 5134
- Napolitano, L., Castellano, M., Pentericci, L., et al. 2025a, *A&A*, 693, A50
- Napolitano, L., Castellano, M., Pentericci, L., et al. 2025b, *ApJ*, 989, 75
- Napolitano, L., Pentericci, L., Dickinson, M., et al. 2025c, arXiv e-prints, arXiv:2508.14171
- Narayanan, D., Torrey, P., Stark, D., et al. 2025, arXiv e-prints, arXiv:2509.18266
- Peng, C. Y., Ho, L. C., Impey, C. D., & Rix, H.-W. 2002, *AJ*, 124, 266
- Pérez-González, P. G., Costantin, L., Langeroodi, D., et al. 2023, *ApJ*, 951, L1
- Pérez-González, P. G., Östlin, G., Costantin, L., et al. 2025, *ApJ*, 991, 179
- Perrin, M. D., Sivaramakrishnan, A., Lajoie, C.-P., et al. 2014, in *Society of Photo-Optical Instrumentation Engineers (SPIE) Conference Series*, Vol. 9143, *Space Telescopes and Instrumentation 2014: Optical, Infrared, and Millimeter Wave*, ed. J. M. Oschmann, Jr., M. Clampin, G. G. Fazio, & H. A. MacEwen, 91433X
- Planck Collaboration, Aghanim, N., Akrami, Y., et al. 2020, *A&A*, 641, A6
- Rodighiero, G., Bisigello, L., Iani, E., et al. 2023, *MNRAS*, 518, L19
- Santini, P., Castellano, M., Calabrò, A., et al. 2025, arXiv e-prints, arXiv:2512.09139
- Somerville, R. S., Yung, L. Y. A., Lancaster, L., et al. 2025, *MNRAS*, 544, 3774
- Tang, M., Stark, D. P., Mason, C. A., et al. 2025, arXiv e-prints, arXiv:2507.08245
- Taylor, A. J., Kokorev, V., Kocevski, D. D., et al. 2025, *ApJ*, 989, L7